Diamond & Related Materials 150 (2024) 111755

Contents lists available at ScienceDirect

Diamond & Related Materials

journal homepage: www.elsevier.com/locate/diamond

Research on the fabrication of high-quality patterned diamond using femtosecond laser

Junjie Zou [a,1], Qijun Wang [a,1], Wei Shen [a,b,c,d], Sheng Peng [a], Zijun Qi [a], Gai Wu [a,b,c,d,*], Qiang Cao [a,e,**], Sheng Liu [a,b]

[a] The Institute of Technological Sciences, Wuhan University, Wuhan 430072, China
[b] School of Power and Mechanical Engineering, Wuhan University, Wuhan 430072, China
[c] Hubei Key Laboratory of Electronic Manufacturing and Packaging Integration, Wuhan University, Wuhan 430072, China
[d] Wuhan University Shenzhen Research Institute, Shenzhen 518057, China
[e] Department of Physics, Qingdao University of Science and Technology, Qingdao 266061, China

ARTICLE INFO

Keywords:
Diamond
Femtosecond laser processing
Micro-nano structures
High-quality fabrication

ABSTRACT

Diamond, known for its exceptional thermal, electrical, and mechanical properties, is widely used in precision machining tools, MEMS, and electronic devices. However, because of its extreme hardness and chemical inertness, diamond machining is highly challenging. Femtosecond laser technology, with its high instantaneous energy and minimal heat-affected zone, has emerged as an effective method for the precision machining of diamond. This study explores the application of 1026 nm and 513 nm femtosecond lasers in diamond grooving. The experimental results indicate that with increasing laser energy density, both groove width and depth increase, accompanied by a rise in amorphous carbon and graphite contents, resulting in increased tensile stress and decreased crystallinity in the machined region. Notably, the 513 nm laser demonstrates higher precision, achieving narrower grooves suitable for fine machining of diamond. Molecular dynamics simulations and experimental data reveal that the formation of amorphous carbon and graphite phases is the primary mechanism for deep ablation, and no significant anisotropy is observed during the process, allowing for the uniform fabrication of micro-nanostructures. TEM analysis confirms the presence of amorphous carbon and nanocrystalline diamond at the groove bottom, indicating phase transformation and also the formation of nanoscale diamond particles in regions of concentrated femtosecond laser energy. This study provides experimental and theoretical support for the high-quality fabrication of micro-nano structures on diamond, with significant implications for its advanced applications.

1. Introduction

Diamond exhibits exceptional thermal, electrical, and mechanical properties due to its high Young's modulus, thermal conductivity, and low thermal expansion coefficient [1–4]. With significant advancements in diamond growth technology, the production cost of synthetic diamond has been greatly reduced compared to natural diamond, thereby broadening its application scope. Synthetic diamond is now extensively utilized in ultra-precision machining tools [5], components for Micro-Electro-Mechanical Systems (MEMS) [6], robust gratings [7], inert and stable medical coatings [8–10], and electronic devices for harsh environments [11–15].

However, the extreme hardness, brittleness, and chemical inertness of diamond pose significant challenges for machining. Traditional methods, such as grinding [16], Electrical Discharge Machining (EDM) [17,18], and abrasive water jet [19], are inefficient and time-consuming when processing this superhard material. Commonly micro-nanostructure processing methods, such as electron beam lithography, photolithography, and reactive ion beam etching, can achieve nanometer-level precision but require complex multiple steps, including film preparation, masking, etching, and cleaning. Furthermore, these techniques often demand stringent processing environments, such as

* Corresponding author at: G. Wu, The Institute of Technological Sciences, Wuhan University, Wuhan 430072, China.
** Corresponding author.
E-mail addresses: wugai1988@whu.edu.cn (G. Wu), caoqiang@whu.edu.cn (Q. Cao).
[1] Junjie Zou and Qijun Wang contributed equally to this work.

https://doi.org/10.1016/j.diamond.2024.111755
Received 27 August 2024; Received in revised form 15 October 2024; Accepted 4 November 2024
Available online 6 November 2024

vacuum conditions, and the choice of materials is limited. Additionally, the etching speed is relatively slow, typically only a few micrometers per hour[20,21]. In contrast, laser processing, as a direct-write technology, can be applied directly to the surface or interior of materials, enabling material removal through ablation. Under certain conditions, laser processing can also achieve nanometer-level precision, with a longitudinal removal rate of several micrometers per second, significantly improving processing efficiency[22].

Laser processing, a non-contact technique, has proven to be an effective method for diamond machining. Although nanosecond lasers are well-established for drilling and cutting [23,24], their large heat-affected zone limits their suitability for precise optical and electronic applications. In contrast, ultrashort-pulse lasers, particularly femtosecond lasers, enable fine micro/nanoscale machining with minimal thermal damage, expanding the potential applications of diamond in optics, electronics, and biomedicine.

In recent years, femtosecond lasers, as a rapidly advancing optical technology, have achieved significant progress in their application to diamond materials. For instance, femtosecond lasers have been utilized in the study of diamond NV color centers [25–27], the fabrication of nanochannels[28], the exploration of stealth dicing within diamond [29,30], X-ray dosimeters [12], particle detectors [13], solar absorbers [14], thermionic devices [15]. and as a precise cutting tool [31]. Furthermore, the formation of microstructures on substrate surfaces has been shown to reduce dislocation density in subsequent film growth which has been demonstrated in the growth of III-*V* semiconductor materials [32]. Thus, investigating the effects of femtosecond lasers on diamond materials is crucial for improving diamond surface structures, enhancing material quality, and expanding its potential for high-end applications.

Femtosecond laser technology has become relatively mature in the field of diamond surface micro-nanostructure processing [33]. Different wavelengths of femtosecond lasers have significant effects on the size and microstructure of diamond [34], and are prone to inducing amorphous carbon and graphitization during processing [35]. Mazur successfully prepared periodic linear grooves on single crystal diamond for the first time using the laser-induced periodic surface structure (LIPSS) technique[36]. In contrast, Trucchi' s group employed single-beam and delayed cross-polarized dual-beam pulsed femtosecond lasers to create periodic stripes and two-dimensional periodic nanostructures on diamond, respectively[37–40]. These studies demonstrate that during laser processing, parameters such as wavelength, number of pulses, and energy density significantly affect the surface morphology, stress in the processed area, crystal quality, and phase transformations of diamond. However, these studies only address certain aspects of how laser processing conditions influence diamond processing, and there remain deficiencies in understanding the mechanisms of laser-diamond interaction, as well as in conducting a more microscopic and detailed analysis of the processing region.

In this study, femtosecond lasers with 1026 nm and 513 nm were used to groove diamond, and a detailed analysis was conducted on the morphology and Raman spectra of the processed regions, focusing on their influence on groove width, depth, stress, and crystallinity. The results indicate that increasing the energy density leads to wider and deeper grooves, accompanied by an increase in amorphous carbon and graphite content, higher tensile stress, and reduced crystallinity. The thresholds for strong and weak ablation of diamond by femtosecond lasers are also determined. The 513 nm laser demonstrated superior precision in machining with narrower grooves. Based on this deeper understanding, suitable processing parameters can be selected as needed, Furthermore, low-energy, multiple processing was shown to result in lower stress and higher crystal quality, enabling the fabrication of high-quality diamond grid structures. This paper further explores the effects of various laser parameters on diamond microstructures by combining molecular dynamics simulations with experimental results. Transmission Electron Microscopy (TEM) analysis revealed the formation of amorphous carbon and nanocrystalline diamond at the groove bottom. Consequently, this paper can provide valuable insights into the fabrication of high-quality micro-nano structures on diamond surfaces.

2. Experiments and methods

2.1. Materials

The diamond used in the experiment was purchased from Zhongnan Diamond Co., Ltd., with specifications of 3 mm × 3 mm × 0.3 mm. It is a type IIa single-crystal diamond synthesized under high temperature and high pressure. The (001) crystal surface of the sample was polished to achieve a surface roughness of less than 1 nm. Before the experiment, the diamond samples were sonicated in acetone, ethanol, and deionized water for 10 min respectively, and then dried with nitrogen gas for use.

2.2. Femtosecond laser processing system

In this experiment, the femtosecond laser processing system is equipped with a Yb: KGW laser (PHAROS, Light Conversion), which generates laser pulses with a wavelength of 1026 nm, a pulse duration of 190 fs, and a repetition rate of 200 kHz. After frequency doubling via a harmonic generator, the system can produce green light with a wavelength of 513 nm. The laser pulse energy is precisely controlled by an electro-optic attenuator, and the polarization direction is fixed by a polarizer and maintained constant throughout the experiment. The laser beam, after passing through a series of mirrors, is focused by a 50× objective lens with a numerical aperture (NA) of 0.42. Consequently, the spot size of the 513 nm wavelength laser is approximately 1.5 μm, whereas the spot size of the 1026 nm wavelength laser is about 3 μm.

A motorized 3D displacement stage (ANT-PLUS series) with a movement accuracy of 0.25 μm was used to precisely control the sample's movement during the patterning of the diamond surface. Additionally, the system uses white light emitted from LEDs to illuminate the sample, and an integrated CCD monitors changes in the diamond sample in real-time, aiding in the optimization of experimental parameters. The schematic diagram of the femtosecond laser processing system is shown in Fig. 1(a). For the experiments, we selected the constant density processing mode, which controls the number of femtosecond laser pulses per unit length. Considering the differences in spot diameters between the 513 nm and 1026 nm lasers, the respective spot densities in this mode are 3000 and 1500, with a constant processing speed of 0.3 mm/s. This means that over a distance of 0.3 mm, the total number of laser pulses was 3000 for the 513 nm laser and 1500 for the 1026 nm laser. All processing operations were conducted in a standard air environment.

2.3. Characterization equipment and methods

To characterize the crystallographic quality of the diamond samples, X-ray diffraction (XRD) rocking curves were measured using a SmartLab diffractometer (Rigaku Inc.). Ultraviolet absorption spectroscopy (UV-2600i, Shimadzu) was employed to obtain the absorption and transmission spectra of the diamond samples. The grid and groove morphology of the diamond samples were analyzed using a 3D optical profiler (NewView 9000, Zygo Inc.). Scanning electron microscope (SEM) images of the machined surface areas were captured with a field emission scanning electron microscope (FE-SEM, Hitachi SU8010). Before SEM imaging, a thin gold (Au) layer was sputter-coated onto the samples at a current of 10 mA for 90 s to enhance electrical conductivity. Prior to TEM sample preparation, the samples were treated in a strong oxidizing solution (H_2SO_4:$HClO_4$:HNO_3 = 1:1:1) at 100 °C for 15 min, followed by ultrasonic cleaning to remove any residues and non-diamond components. TEM samples were then prepared using focused ion beam (FIB) cutting, This cutting process was performed along the (110) crystal plane, which is perpendicular to the (100) plane. With gold

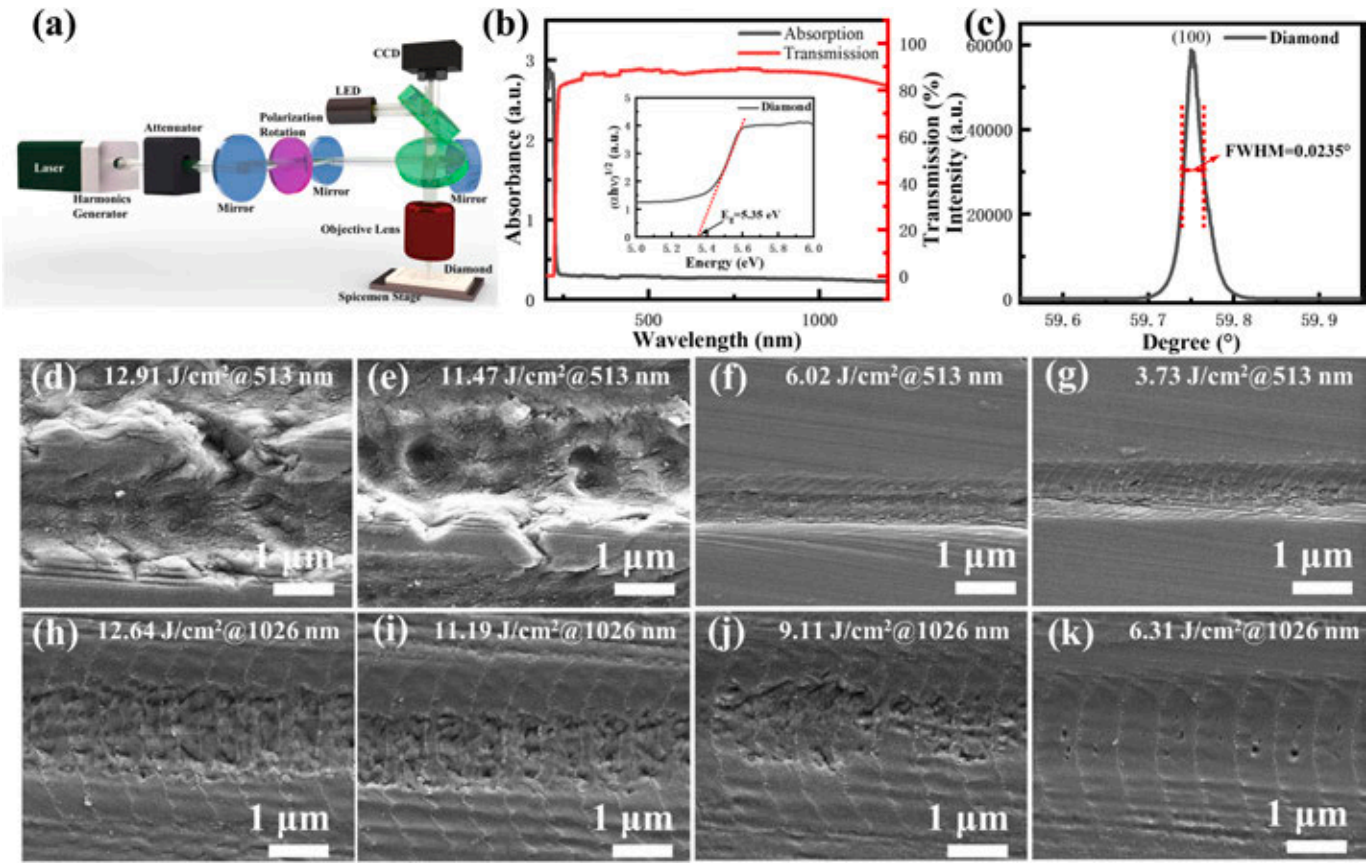

Fig. 1. (a) Schematic diagram of the femtosecond laser processing system; (b) UV–Vis absorption spectra of the diamond samples, with the inset showing the Tauc plot for determining the bandgap of the diamonds; (c) X-ray diffraction (XRD) pattern of the diamond; SEM images of the processing regions using a 513 nm femtosecond laser at different average energy densities: (d) 12.91 J/cm^2; (e) 11.47 J/cm^2; (f) 6.02 J/cm^2; (g) 3.73 J/cm^2; SEM images of the processing regions using a 1026 nm femtosecond laser at different average energy densities: (h) 12.64 J/cm^2; (i) 11.19 J/cm^2; (j) 9.11 J/cm^2; (k) 6.31 J/cm^2.

(Au) as the conductive layer and platinum (Pt) deposited to protect the sample surface from ion beam damage.

The micro-Raman spectra of the processed diamond areas and substrates were measured using a LabRAM HR Evolution spectrometer (HORIBA). The excitation wavelength was set to 633 nm, and the device was configured with a grating of 1800 lines/mm, focusing through a 100× objective lens. The spectrometer's resolution was approximately 0.65 cm^{-1}. Before test, the device was calibrated using the Raman peak of single-crystal silicon at 520.7 cm^{-1}.

2.4. Molecular dynamics simulation

The Large Scale Atomic/Molecular Massively Parallel Simulator (LAMMPS) was used for molecular dynamics (MD) simulations [41]. The MD model consists of a single-crystal diamond lattice and a laser energy field, with their spatial relationship illustrated in Fig. S1. The lattice model has dimensions of 160 Å in the x and y directions and 150 Å in the z direction, with the x, y, and z axes corresponding to the [100], [010], and [001] crystal orientations, respectively. The model size was reduced to balance computational cost with the validity of the simulation results. An optimized diamond lattice was generated using the conjugate gradient method [42]. The model was then sequentially relaxed using the NPT and NVT ensembles with a relaxation time of approximately 20 ps, resulting in an initial diamond structure at 300 K, which was then transitioned to the NVE ensemble during the laser input stage. The modified Velocity-Verlet algorithm was employed to integrate the Newtonian eqs. [43]. The Tersoff potential, an interatomic potential of the covalent bonding type, was used in this model to describe the hybridization of C—C bonds and the phase transition between diamond and graphite. This potential not only allows for the calculation of lattice constants, bond energies, bond angles, elastic moduli, and vacancy formation energies but also describes the dynamics of chemical bond formation and breakage, as well as changes in interatomic bonding within the system [44]. The time step for the calculations was set to 0.1 fs.

The theory of femtosecond pulsed laser-material interaction describes the physical process by which diamond absorbs femtosecond pulsed laser energy. When a diamond is exposed to the intense electromagnetic field of a femtosecond laser, Diamond materials can induce electron transitions to higher energy levels through multiphoton absorption. This process typically triggers photoionization, which mainly involves mechanisms such as multiphoton ionization, tunneling ionization, and avalanche ionization[45]. Subsequently, these hot electrons undergo relaxation and recombine with holes, transferring the photon energy to the lattice and leading to the material's melting or vaporization. This energy transfer process is nonlinear. However, the behavior of electrons falls outside the scope of classical molecular dynamics (MD) simulations. As a result, the nonlinear energy absorption process modeled in MD simulations may not fully capture the experimental outcomes of femtosecond laser direct writing. The shape of the laser propagation region within the diamond lattice is illustrated in Fig. S1(a). According to experimental observations, the laser source used resembles an inverted cone. While the model simplifies the nonlinear energy absorption process and has limitations in explaining the precise physical mechanisms of femtosecond laser processing of diamond, it remains effective in elucidating the structural changes within the material.

3. Results and discussion

3.1. Exploration of groove micromachining

Fig. 1(a) presents a schematic diagram of the femtosecond laser processing system utilized in the experiment. The system employed a laser with a wavelength of 1026 nm, a pulse duration of 190 fs, and a repetition frequency of 200 kHz. This 1026 nm laser was frequency-doubled to produce a laser with a wavelength of 513 nm.

Fig. 1(b) presents the UV–Vis-IR absorption spectra of the single-crystal diamond samples used in the experiments. The spectra reveal that the diamond samples exhibit higher transmittance and lower absorption at both 1026 nm and 513 nm, with absorption coefficients and transmittance at 513 nm being slightly higher than those at 1026 nm. The inset presents the Tauc plot for the diamond, from which the bandgap energy is determined to be 5.35 eV. This value is lower than the 5.46–5.5 eV range reported in the literature, likely due to minor impurities or crystal defects in the sample. These factors can influence the band structure, leading to slight variations in the band gap. This suggests that both the 513 nm and 1026 nm lasers used in the experiment interact with the diamond through a multiphoton ionization mechanism. Fig. 1 (c) displays the rocking curve of the (100) crystal plane of the diamond sample. The (100) crystal plane is positioned at 59.75°, with a full width at half maximum (FWHM) of 0.0235°, indicating that the diamond sample possesses high crystallographic quality.

To achieve high-quality machined morphology and dimensions when processing single-crystal diamond, a femtosecond laser processing method based on spot density was employed. Specifically, the number of femtosecond laser pulses per unit time was controlled at a constant scanning speed to ensure equal time intervals between individual pulses, thereby regulating the overlap between spots. Given that the spot diameter of the 513 nm is approximately half that of the 1026 nm, the processing speed was set to 0.3 mm/s. The spot densities for the 1026 nm and 513 nm lasers were 1500 and 3000, respectively. This indicates that the total number of laser pulses at a distance of 0.3 mm is 1500 for the 1026 nm laser and 3000 for the 513 nm laser. Under these conditions, the effects of different wavelengths and energy densities on the machined morphology were investigated.

Diamond selectively absorbs 513 nm and 1026 nm lasers, with the 513 nm laser exhibiting higher single-photon energy. At the same energy density, laser processing at these different wavelengths results in distinct morphological features. Fig. 1(d)-(g) and (h)-(k) illustrate the surface morphology of grooves machined with 513 nm and 1026 nm lasers at varying energy densities, respectively. The results indicate that at high energy densities—approximately 12 J/cm^2 for the 513 nm laser and 11 J/cm^2 for the 1026 nm laser—the surface processed with the 513 nm laser is more concave and uneven compared to the surface processed with the 1026 nm laser. This difference may be attributed to the more intense ablation effect of the 513 nm laser under high power conditions, leading to greater material removal and poorer localized morphology. In contrast, at lower power conditions, the 513 nm laser exhibits weaker ablation, resulting in more controllable morphology with flatter groove bottoms and better-defined edges, thereby improving machining quality [46–48]. Consequently, the high-power 513 nm laser is less suitable for processing diamond. Nevertheless, the 513 nm laser achieves a smaller groove width compared to the 1026 nm laser, making it more appropriate for the fine processing of diamond microstructures. Fig. S2 presents SEM images of the diamond surface at various average energy densities with a 513 nm wavelength and a spot density of 1500. It reveals that, as energy density increases, deeper but discontinuous pits develop on the diamond surface. Conversely, at a spot density of 3000, the surface does not exhibit significant pits or poor morphology even at high energy densities. Thus, increased spot density results in greater heat accumulation per unit area, which is a crucial factor influencing machining quality.

Fig. 2(a) illustrates the relationship between groove width and average energy density. For the 1026 nm wavelength laser, when the average energy density is below 6.31 J/cm^2, the width of the grooves increases with energy density. However, above 6.31 J/cm^2, the increase in groove width levels off, reaching a maximum of approximately 3.87 μm at 14.61 J/cm^2. For the 513 nm wavelength laser, the groove width remains relatively stable, fluctuating between 1.78 and 1.99 μm when the energy density is below 7.75 J/cm^2. Beyond this energy density, the groove width shows more pronounced fluctuations.

Fig. 2(b) illustrates the variation in groove depth with average energy density. The figure shows that groove depth increases with average energy density for both the 1026 nm and 513 nm lasers. At energy densities below 5.16 J/cm^2, the groove depth is greater for the 1026 nm wavelength laser compared to the 513 nm wavelength laser. Conversely, at energy densities above 5.16 J/cm^2, the groove depth becomes greater for the 513 nm wavelength laser. Notably, for the 513 nm wavelength, the groove depth exhibits more fluctuation at energy densities exceeding 7.75 J/cm^2, which is attributed to difficulties in controlling groove structure and deterioration in morphology under high energy density conditions. This indicates that 7.75 J/cm^2 represents a threshold between strong and weak ablation for the 513 nm laser.

3.2. Raman spectroscopy analysis of groove structures

Raman spectroscopy, a widely used non-destructive characterization technique, can be employed with a microscopy system to analyze crystallographic quality, stress, and the introduction of non-diamond phases in regions processed by femtosecond lasers. Fig. 3(a) and (d) present the normalized Raman spectra of the machined grooves at various average

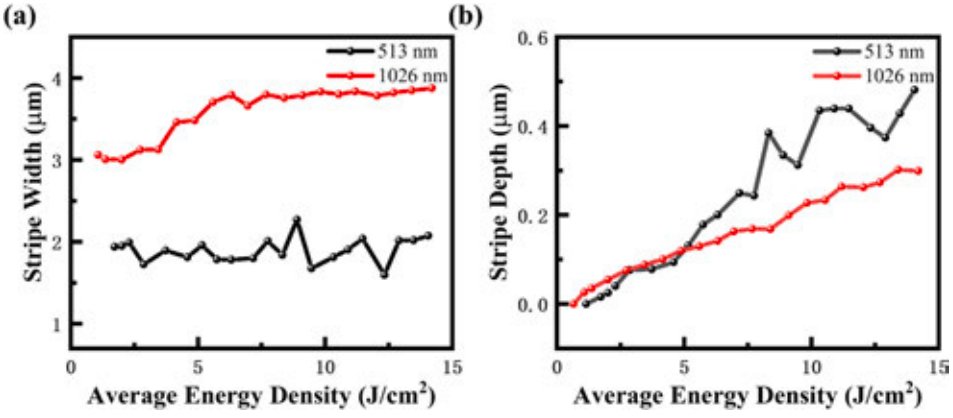

Fig. 2. (a) the variation in groove width at different average energy densities for 513 nm and 1026 nm wavelengths; (b) the variation in groove depth at different average energy densities for 513 nm and 1026 nm wavelengths.

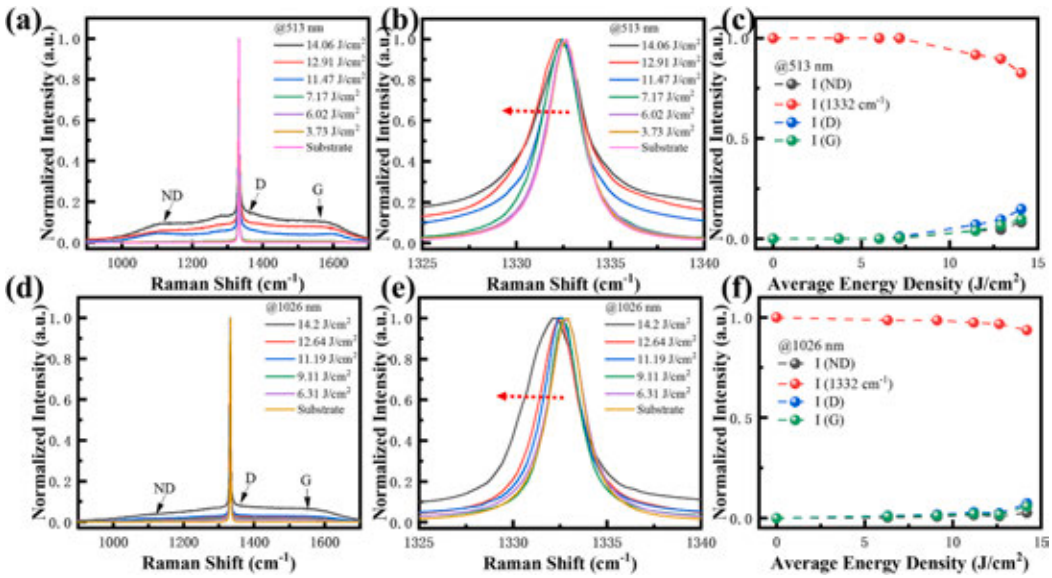

Fig. 3. (a) and (d) the normalized Raman spectra of the processed grooves for the 513 nm and 1026 nm lasers at various average energy densities, (b) and (e) enlarged views of the normalized Raman spectra of the processed grooves for the 513 nm and 1026 nm lasers at various average energy densities. (c) and (f) the trends in peak positions for the processed grooves using the 513 nm and 1026 nm lasers at various average energy densities.

energy densities for the 513 nm and 1026 nm lasers, respectively. As the average energy density increases, there is a notable rise in background intensity in the range of 900–1700 cm^{-1}, attributed to nanocrystalline diamond (ND) and sp^2-bonded carbon, the diamond intrinsic peak, the D-band, and the G-band, respectively [49–52]. At the same energy density, the increase in intensity is more pronounced for the 513 nm laser compared to the 1026 nm laser. The Fig. 3(b) and (e) illustrate that the diamond characteristic peaks shift to lower wavelengths with increasing energy density, accompanied by an increase in the full width at half maximum (FWHM) of these peaks.

By fitting the Raman spectra (Figs. S1 and S2), The peaks located at approximately 1120 cm^{-1}, 1332 cm^{-1}, 1350 cm^{-1}, and 1565 cm^{-1} were identified, corresponding to nanocrystalline diamond (ND) and sp^2-bonded carbon, the diamond intrinsic peak, the D-band, and the G-band, respectively [49–52]. The variations in their normalized intensities are shown in Tables S1 and S2, while the trends in peak positions are depicted in Fig. 3(c) and 3(f). Our analysis shows that the intensity of the 1332 cm^{-1} peak (I(1332 cm^{-1})) decreases with increasing laser energy density, whereas the intensities of the ND peak (I(ND)), the D-band (I (D)), and the G-band (I(G)) increase. The intensity change in the D-band is larger than that of the G-band, and the change in the G-band is larger than that of the ND peak. This indicates that when the laser energy density exceeds a certain threshold, part of the diamond structure transforms, forming ND, D-band, and G-band features. For the 513 nm laser, this threshold is around 7 J/cm^2, while for the 1026 nm laser, the threshold is around 11 J/cm^2. As the energy density increases further, the intensities of these non-diamond phases increase more significantly. Therefore, controlling the energy density during processing can effectively minimize the generation of non-diamond phases.

By performing Lorentzian fitting of the Raman spectra, the peak positions and full width at half maximum (FWHM) of the characteristic peaks of the processed diamond can be accurately determined, allowing for further analysis of the stresses in the machined grooves and the crystallographic quality of the diamond. The peak positions and FWHM values at various energy densities are presented in Fig. 4(a) and (b). The results indicate that as the energy density increases, the Raman peak positions shift to lower wavenumbers for both 513 nm and 1026 nm lasers, signifying the presence of tensile stress [53]. When the energy density is below 5 J/cm^2, the grooves processed with the 1026 nm laser exhibit some compressive stress. Overall, the trend observed at 1026 nm is less pronounced compared to 513 nm. The FWHM of the Raman spectra increases with higher energy density, reflecting a deterioration in the crystallographic quality of the diamond. Notably, the FWHM increases significantly when the energy density exceeds 7.75 J/cm^2, with the FWHM being generally higher at 513 nm compared to 1026 nm. This indicates a more pronounced degradation in crystallographic quality at

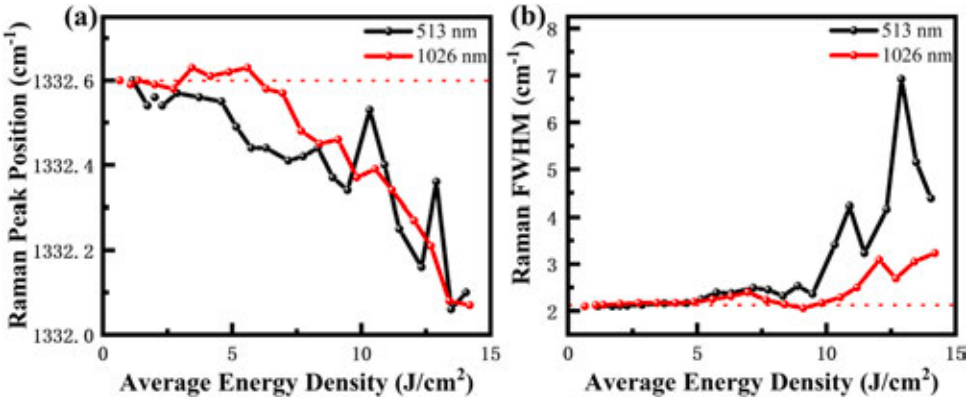

Fig. 4. (a) and (b) the variations in peak positions and full-width at half-maximum (FWHM) of the Raman spectra at different average energy densities.

the shorter wavelength. Additionally, significant fluctuations in the characteristic peaks and FWHM are observed for diamond grooves processed with the 513 nm wavelength when the energy density exceeds 7.75 J/cm^2. Therefore, the accumulation of internal stresses and the deterioration of crystallographic quality are key factors contributing to the degradation of diamond groove quality.

Therefore, laser processing of diamond at both 513 nm and 1026 nm wavelengths with high energy densities substantially degrades the crystallographic quality and induces significant compressive stresses within the diamond. High-quality surface patterned structures can be achieved using both 513 nm and 1026 nm lasers with appropriate control of the processing parameters. However, for achieving finer and higher-quality surface microstructures, the 513 nm wavelength is the optimal choice.

3.3. Exploration of grid machining parameters

To achieve high-precision and high-quality processing of diamond morphology, selecting the appropriate wavelength and energy density is crucial. Processing with a 513 nm laser yields higher accuracy compared to a 1026 nm laser. At high energy densities, graphitization and internal tensile stress in the diamond become more pronounced, potentially leading to defects such as cracks and chipping in the machined areas. These issues can significantly impact the quality of the processed morphology.

Fig. 5(a)-(d) shows optical images of diamond samples processed at a high energy density of 6.02 J/cm^2 for 1, 2, 3, and 5 times. Fig. 5(e) and (f) display optical images of samples processed at a lower energy density of 2.87 J/cm^2 for 5 and 10 times. The images reveal that the edge morphology deteriorates progressively with an increasing number of processing times at high energy density, resulting in uncontrollable and irregular shapes. Conversely, at the lower energy density, the edge morphology of the grid remains regular and well-defined, even after multiple processing times. Therefore, to achieve high-quality processing results, it is advisable to perform multiple processing times at a lower energy density of 2.87 J/cm^2. Fig. S5 presents a zoomed-in SEM image of the processed grid area, showing grooves formed after multiple processing times, "Junction" where horizontal and vertical processing overlap, and unprocessed "Grid" sections. The image confirms that the groove edge structure remains intact.

Laser-induced periodic surface structures (LIPSSs) can be observed in Figs. S3 and S4. SEM characterization of the groove and junction points is presented in Fig. S6(a) and (b). The LIPSS patterns are aligned along the Y axis. Additionally, we conducted two-dimensional fast Fourier transform (2D-FFT) analysis on the groove region (region c), the region between the groove and the junction (region d), and the junction region (region e), with the results shown in Fig. S6(c)–(e) [40]. The analysis reveals that the distance between the central bright spots remains nearly constant, indicating that the periodic structure is consistent across the groove region, junction region, and connection point, with a period of approximately 140 nm. In Fig. 1, the SEM image shows that LIPSS is almost absent in the groove machining region. This could be because the laser scanning direction is along the X-axis, while the growth direction of LIPSS is along the Y-axis, which are perpendicular to each other. As a result, with fewer processing passes, the formation of LIPSS is difficult to observe in the groove region scanned along the X-axis.

By analyzing the Raman spectra for different numbers of processing times, the relationship between the Raman peak position and full width at half maximum (FWHM) has been derived, as shown in Fig. 6 (a) and (b). These figures display the variation in Raman peak position and FWHM, respectively, at an average energy density of 6.024 J/cm^2. The red dashed line indicates the peak position and FWHM of the diamond substrate. As seen in the figures, when the number of processing times is 2 or fewer, the Raman peak position shifts toward higher wavenumbers. However, as the number of processing times increases, the Raman peak position shifts toward lower wavenumbers overall. The FWHM of the lattice region gradually decreases with increasing processing times, indicating an improvement in crystalline quality. In contrast, the FWHM of the groove region increases with additional processing times, suggesting a decline in crystalline quality in that region. Notably, when the number of processing times is fewer than 2, the FWHM of the grooves is smaller than that of the grid, indicating better crystalline quality. Additionally, the FWHM of the connection point, which has undergone twice as many processing times as the grooves, is overall higher than that of the grooves and reaches a maximum after 3 processing times.

Fig. 6 (c) and (d)shows the changes in Raman peak position and full-

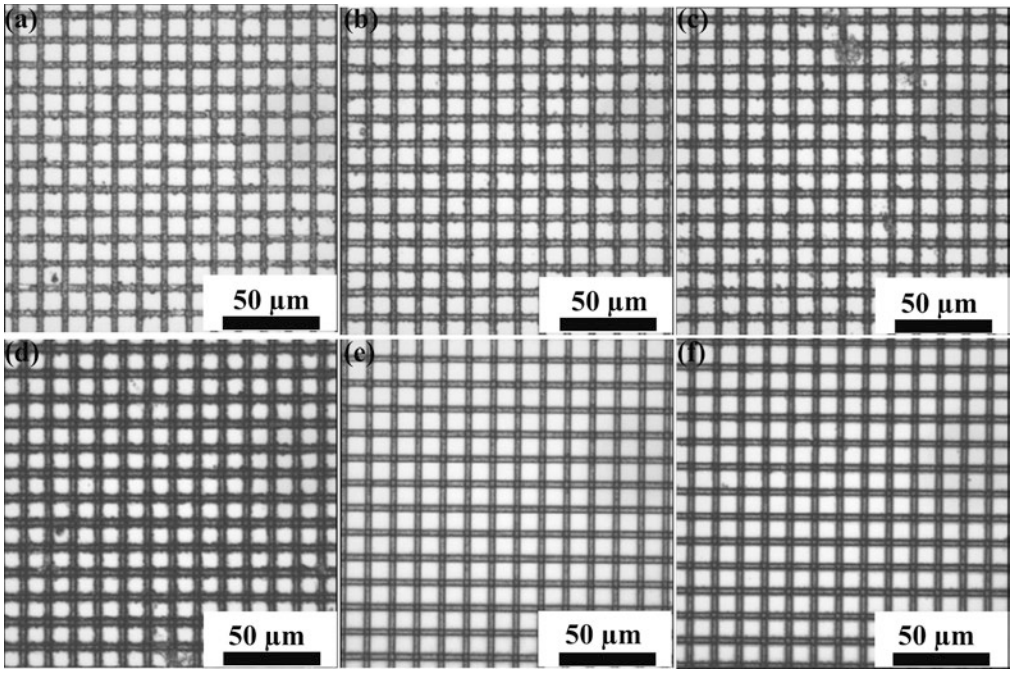

Fig. 5. Optical microscope images of diamond samples processed with varying numbers of times at different energy densities: (a) 1 time, (b) 2 times, (c) 3 times, and (d) 5 times at an energy density of 6.02 J/cm^2; (e) 5 times and (f) 10 times at an energy density of 2.87 J/cm^2.

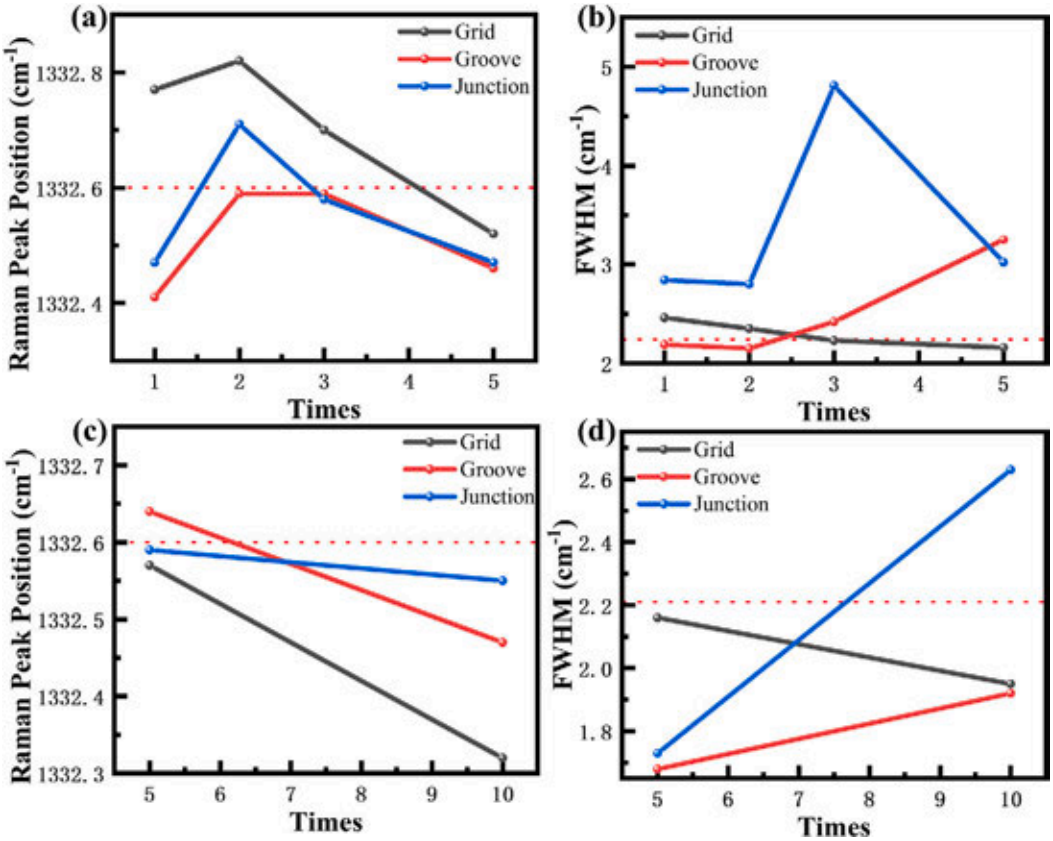

Fig. 6. The impact of processing times on Raman peak position and full width at half maximum (FWHM) under different energy densities. (a) and (b) the effects at an average energy density of 6.024 J/cm^2, (c) and (d) show the results at an average energy density of 2.868 J/cm^2.

width at half-maximum (FWHM) for a low average energy density of 2.87 J/cm^2. It is evident that, with 10 processing times compared to 5 times, the Raman peak position shifts significantly toward lower wavenumbers, indicating the accumulation of stresses even under low-power processing conditions. This stress accumulation can lead to chipping at the edges of the samples. Additionally, while the FWHM of the grid decreases, both the grooves and junction exhibit an increasing trend in FWHM. This suggests that the crystallographic quality is better with fewer machining times, as indicated by the smaller FWHM values for both the grooves and joints at lower numbers of processing times.

Therefore, to minimize chipping at the groove edges caused by stress accumulation while avoiding significant damage to the diamond crystal structure, it is optimal to use low-energy multiple machining conditions for surface microstructure fabrication.

Fig. 7 illustrates the relationship between groove depth and processing times under different energy densities. The data reveal that, at energy densities of 6.02 J/cm^2 and 2.87 J/cm^2, there is a roughly linear increase in groove depth with the number of processing times. The 3D profiles are shown in Fig. S7 and Fig. S8, respectively. In contrast, the width of the grooves remains relatively constant. This suggests that increasing the number of machining times effectively deepens the grooves, but may also lead to chipping of the grid edges and subsequent deterioration of the morphology. Therefore, it is crucial to balance the trade-off between groove depth and width when optimizing the machining process.

Fig. 8(a)-(e) displays the molecular dynamics simulations of diamond depth changes under varying numbers of laser processing times. The simulations reveal that during the initial processing, the ablation depth of the diamond changes minimally, with most of the area undergoing phase transitions, resulting in the formation of amorphous carbon and graphite. As processing continues, some of this modified layer is removed through further laser ablation, while a new modified layer forms. This results in an overall increase in both the ablation depth and the modified depth of the diamond. The data show a decreasing trend in modification depth with increasing processing times, while the ablation depth increases almost linearly with the number of processing steps, consistent with the observed processing effects in Fig. 7. Although diamond is known for its exceptional hardness, its interaction with the laser causes it to become susceptible to modification and ablation due to the formation of modified layers (i.e., amorphous carbon and graphite).

To investigate the effect of crystallographic orientation on diamond machining, the process was performed in two distinct directions: parallel to the sample edge (0°, corresponding to the [001] crystal orientation) and at an angle of 45° (corresponding to the [110] crystal orientation), as illustrated in the schematic in Fig. S10(a). Fig. S10(b) presents contour plots for the 0° and 45° machining directions. The results indicate that the length and width of the grooves are identical for both directions under the same machining parameters, measuring 0.5 μm and 4.17 μm, respectively. This suggests that diamond surface machining is not influenced by crystal anisotropy, which aligns with the molecular dynamics simulations discussed previously. Fig. S10(d) and (g) display optical microscope images for the 0° and 45° directions, respectively, while Fig. S10(c)-(e) and (f)-(h) provide 3D contour maps for the same directions. The images and contour maps show that the lattice edges remain horizontal and vertical without chipping under low-energy multiple processing conditions, indicating that the machining profile is unaffected by the crystallographic orientation. This observation is consistent with the molecular dynamics simulations of diamond processed along different crystallographic orientations, as shown in Fig. S11.

Additionally, grooves with a width of 10 μm and arrays of microdisks with a diameter of 10 μm were machined under identical parameter conditions. Both types of features exhibited high machining quality, as illustrated in Fig. S12.

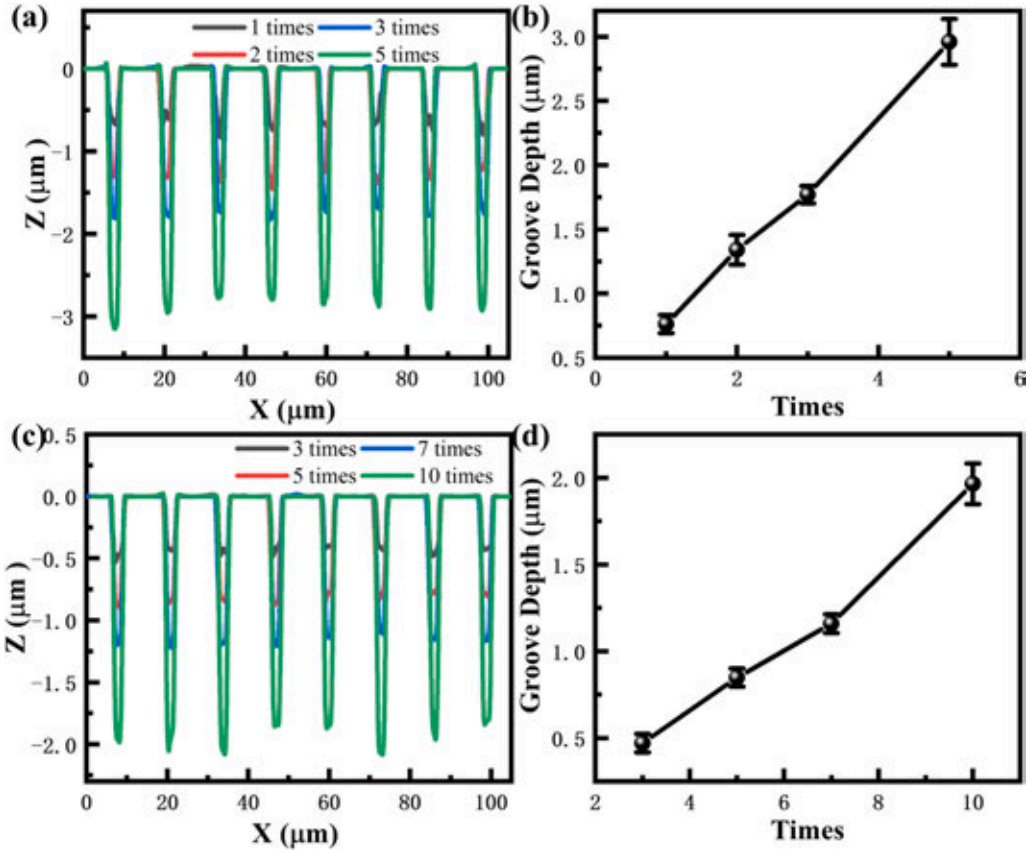

Fig. 7. Statistics on groove depth and regularity for various processing times: (a) and (b) show data for an energy density of 6.02 J/cm^2, (c) and (d) correspond to an energy density of 2.87 J/cm^2.

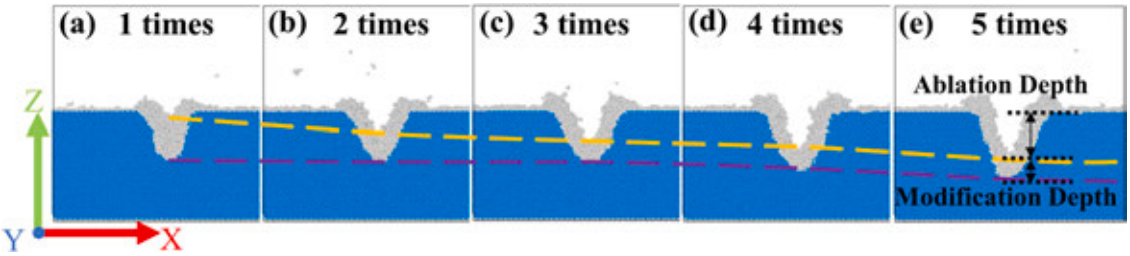

Fig. 8. Molecular dynamics simulations showing the depth changes in diamond after different numbers of laser processing times: (a) 1 time; (b) 2 times; (c) 3 times; (d) 4 times; (e) 5 times.

3.4. TEM analysis of machined grooves and grids

To investigate the impact of femtosecond laser processing on diamond crystallographic quality in detail, high-resolution transmission electron microscopy (TEM) was employed. A laser with a wavelength of 513 nm and an energy density of 2.87 J/cm^2 was used for grid structure fabrication. After 5 times processing, the grid groove width was approximately 3 μm. Following laser processing, the samples were treated in a strong oxidizing solution (H_2SO_4:$HClO_4$:HNO_3 = 1:1:1) at 100 °C for 15 min, followed by ultrasonic cleaning to remove any residues and non-diamond components. The Raman spectra before and after acid cleaning are shown in Fig. S13. For sample preparation, the focused ion beam (FIB) technique was used to section the samples, and a metallic conductive layer (platinum, Pt) was deposited on the surface to protect it. Fig. 9(a) to (c) display images of the samples after FIB cutting. Fig. 9 (d) presents the elemental distribution of the region marked as "d" in Fig. 9(e), highlighting the distinct distribution of carbon (C), gold (Au), and platinum (Pt). The distribution of individual elements is further detailed in Fig. S14.

Fig. 9(f) shows the selected area electron diffraction (SAED) pattern of the sample's "f" region, revealing diffraction spots corresponding to the crystal planes $(1\bar{1}1)$, (002), and $(\bar{1}11)$. This pattern indicates that the sample's [110] zone axis is aligned with these planes. Fig. 9(g)-(i) presents high-resolution transmission electron microscopy (TEM) images of the "g-i" regions of the sample, with insets providing localized zoomed views. These regions correspond to the bottom of the groove, the sidewall of the groove, and the edge of the lattice, respectively. Fig. 9(j)-(l) shows the corresponding fast Fourier transform (FFT) images. The images reveal that the lattice edges and groove sidewalls, which were minimally or not directly irradiated by the laser, exhibit minimal damage. The crystal plane spacing in these regions is measured to be 0.206 nm, corresponding to the diamond (111) plane. In contrast, the bottom of the grooves shows significant lattice disruption due to concentrated laser energy, leading to the formation of a nanocrystalline diamond structure. The FFT images for these areas display, in addition to the diffraction spots of crystallographic phases, a weak "halo ring" around

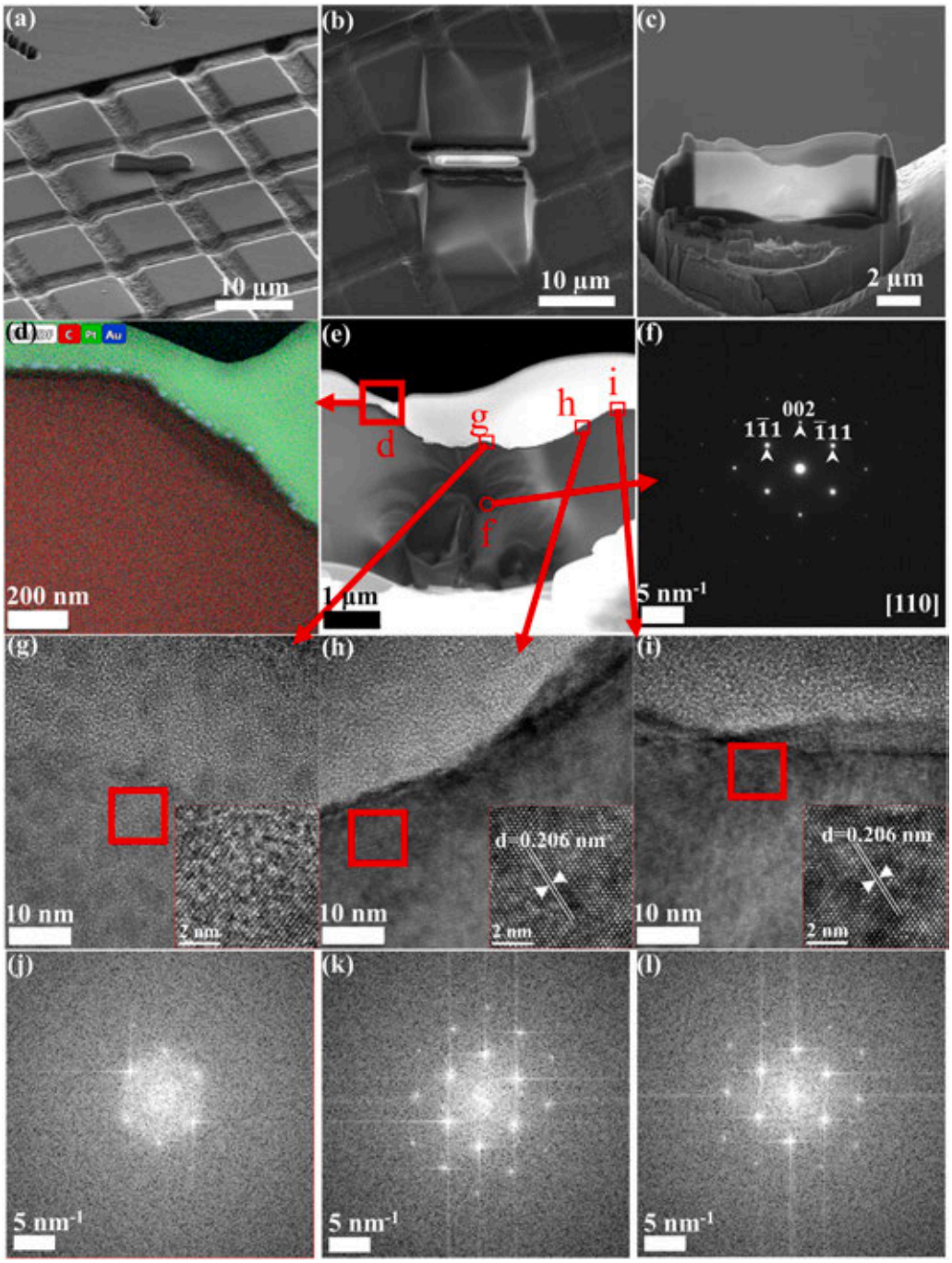

Fig. 9. High-resolution TEM images following femtosecond laser processing: (a) Position of the diamond sample cut with FIB; (b) SEM top view image of the FIB cut surface; (c) Cross-sectional view of the FIB cut sample; (d) Elemental distribution at the interface after laser ablation; (e) TEM cross-sectional view; (f) Selected electron diffraction pattern; (g) and (j) High-resolution TEM and corresponding FFT images of region "g", respectively; (h) and (k) High-resolution TEM and corresponding FFT images of region "h", respectively; (i) and (l) High-resolution TEM and corresponding FFT images of region "l", respectively. Insets in panels (g)-(i) are magnified views of the localized areas in the high-resolution TEM images.

the center of the pattern, indicating the presence of amorphous phases and amorphous carbon [54].

These results provide a detailed description of the effects of femtosecond laser processing on the microstructure of diamond crystals and offer valuable insights for a deeper understanding of the underlying processing mechanisms.

4. Conclusion

In conclusion, this study systematically investigates the effects of energy density on groove morphology, stress state, and material crystallinity during microstructural processing of diamond surfaces using 1026 nm and 513 nm femtosecond lasers. Experimental results demonstrate that the increase of energy density can lead to a significant increase in both the width and depth of grooves, accompanied by the formation of amorphous carbon and graphite. These changes result in increased tensile stress and reduced crystallinity in the groove region. The 513 nm laser, compared to the 1026 nm laser, exhibits superior processing accuracy, particularly under low-energy multiple processing conditions. This results in reduced stress and relatively higher

crystallographic quality in the processed diamond regions. Molecular dynamics simulations further elucidate the mechanism of femtosecond laser processing of diamond, confirming that the generation of amorphous carbon and graphite is crucial for achieving greater ablation depths. Additionally, the simulations reveal that anisotropy effects are minimal, facilitating the formation of diverse micro- and nanostructures. By optimizing processing parameters, high-quality diamond lattice structures were successfully achieved, providing valuable insights into the surface and internal micro-nano processing of other materials.

CRediT authorship contribution statement

Junjie Zou: Writing – original draft, Investigation, Formal analysis, Conceptualization. **Qijun Wang:** Writing – original draft, Investigation, Validation, Conceptualization. **Wei Shen:** Methodology, Visualization, Data curation. **Sheng Peng:** Formal analysis. **Zijun Qi:** Investigation, Validation, Software. **Gai Wu:** Writing – review & editing, Supervision, Project administration, Funding acquisition, Conceptualization, Resources. **Qiang Cao:** Writing – review & editing, Supervision, Funding acquisition, Conceptualization. **Sheng Liu:** Writing – review & editing.

Declaration of competing interest

The authors declared that no conflicts of interest or personal relationships could have appeared to influence the work reported in this paper.

Acknowledgements

This work was funded by the National Natural Science Foundation of China (Grant No. 62004141), the Knowledge Innovation Program of Wuhan-Shuguang (Grant No. 2023010201020243), the Strategic Priority Research Program of the Chinese Academy of Sciences (Grant No. XDA25040201), the Outstanding Youth Foundation of Shandong Province-Taishan Scholar Program (Grant No. tsqn202312207), the Open Fund of Hubei Key Laboratory of Electronic Manufacturing and Packaging Integration (Wuhan University) (Grant No. EMPI2024014), the Qingdao New Energy Shandong Laboratory Open Project (Grant No. QNESL OP 202305), the Fundamental Research Funds for the Central Universities (Grant No. 2042022kf1028), and the China Scholarship Council (Grant No. 202206275005).

Appendix A. Supplementary data

Supplementary data to this article can be found online at https://doi.org/10.1016/j.diamond.2024.111755.

Data availability

The data that support the findings of this study are available from the corresponding author upon reasonable request.

References

[1] C. Raman, The structure and properties of diamond, Curr. Sci. 12 (1943) 33–42.
[2] J.E. Field, The mechanical and strength properties of diamond, Rep. Prog. Phys. 75 (2012) 126505.
[3] Q. Huang, D.L. Yu, B. Xu, W.T. Hu, Y.M. Ma, Y.B. Wang, Z.S. Zhao, B. Wen, J.L. He, Z.Y. Liu, Y.J. Tian, Nanotwinned diamond with unprecedented hardness and stability, Nature 510 (2014) 250-+.
[4] K.E. Spear, J.P. Dismukes, Synthetic Diamond: Emerging CVD Science and Technology, John Wiley & Sons, 1994.
[5] A. Meier, Diamond turning of diffractive microstructures, Precision Engineering-Journal of the International Societies for Precision Engineering and Nanotechnology 42 (2015) 253–260.
[6] Z.L. Cao, D. Aslam, Fabrication technology for single-material MEMS using polycrystalline diamond, Diamond Relat. Mater. 19 (2010) 1263–1272.
[7] P. Forsberg, M. Karlsson, High aspect ratio optical gratings in diamond, Diamond Relat. Mater. 34 (2013) 19–24.
[8] C.H. Wei, K.S. Peng, M.S. Hung, The effect of hydrogen and acetylene mixing ratios on the surface, mechanical and biocompatible properties of diamond-like carbon films, Diamond Relat. Mater. 63 (2016) 108–114.
[9] R.J. Narayan, R.D. Boehm, A.V. Sumant, Medical applications of diamond particles & surfaces, Mater. Today 14 (2011) 154–163.
[10] G.B.J. Cadot, K. Thomas, J.P. Best, A.A. Taylor, J. Michler, D.A. Axinte, J. Billingham, Investigation of the microstructure change due to phase transition in nanosecond pulsed laser processing of diamond, Carbon 127 (2018) 349–365.
[11] C.J.H. Wort, R.S. Balmer, Diamond as an electronic material, Mater. Today 11 (2008) 22–28.
[12] A. Porter, K. Kanxheri, I.L. Paz, A. Oh, L. Servoli, C. Talamonti, A 3D diamond dosimeter with graphitic surface connections, Diamond Relat. Mater. 133 (2023) 109692.
[13] M. Artuso, F. Bachmair, L. Bäni, M. Bartosik, J. Beacham, V. Bellini, V. Belyaev, B. Bentele, E. Berdermann, P. Bergonzo, A. Bes, J.M. Brom, M. Bruzzi, M. Cerv, C. Chau, G. Chiodini, D. Chren, V. Cindro, G. Claus, J. Collot, S. Costa, J. Cumalat, A. Dabrowski, R. D'Alessandro, W. de Boer, B. Dehning, D. Dobos, M. Dünser, V. Eremin, R. Eusebi, G. Forcolin, J. Forneris, H. Frais-Kölbl, K.K. Gan, M. Gastal, M. Goffe, J. Goldstein, A. Golubev, L. Gonella, A. Gorišek, L. Graber, E. Grigoriev, J. Grosse-Knetter, B. Gui, M. Guthoff, I. Haughton, D. Hidas, D. Hits, M. Hoeferkamp, T. Hofmann, J. Hosslet, J.Y. Hostachy, F. Hügging, H. Jansen, J. Janssen, H. Kagan, K. Kanxheri, G. Kasieczka, R. Kass, F. Kassel, M. Kis, G. Kramberger, S. Kuleshov, A. Lacoste, S. Lagomarsino, A. Lo Giudice, C. Maazouzi, I. Mandic, C. Mathieu, N. McFadden, G. McGoldrick, M. Menichelli, M. Mikuž, A. Morozzi, J. Moss, R. Mountain, S. Murphy, A. Oh, P. Olivero, G. Parrini, D. Passeri, M. Pauluzzi, H. Pernegger, R. Perrino, F. Picollo, M. Pomorski, R. Potenza, A. Quadt, A. Re, G. Riley, S. Roe, M. Sapinski, M. Scaringella, S. Schnetzer, T. Schreiner, S. Sciortino, A. Scorzoni, S. Seidel, L. Servoli, A. Sfyrla, G. Shimchuk, D.S. Smith, B. Sopko, V. Sopko, S. Spagnolo, S. Spanier, K. Stenson, R. Stone, C. Sutera, A. Taylor, M. Traeger, D. Tromson, W. Trischuk, C. Tuve, L. Uplegger, J. Velthuis, N. Venturi, E. Vittone, S. Wagner, R. Wallny, J.C. Wang, P. Weilhammer, J. Weingarten, C. Weiss, T. Wengler, N. Wermes, M. Yamouni, M. Zavrtanik, A 3D diamond detector for particle tracking, Nucl. Instrum. Methods Phys. Res., Sect. A 824 (2016) 402–405.
[14] M. Girolami, A. Bellucci, M. Mastellone, S. Orlando, V. Valentini, R.M. Montereali, M.A. Vincenti, R. Polini, D.M. Trucchi, Optical characterization of double-nanotextured black diamond films, Carbon 138 (2018) 384–389.
[15] M. Girolami, L. Criante, F. Di Fonzo, S. Lo Turco, A. Mezzetti, A. Notargiacomo, M. Pea, A. Bellucci, P. Calvani, V. Valentini, D.M. Trucchi, Graphite distributed electrodes for diamond-based photon-enhanced thermionic emission solar cells, Carbon vol. 111 (2017) 48–53.
[16] P.L. Tso, Y.G. Liu, Study on PCD machining, Int. J. Mach Tools Manu. 42 (2002) 331–334.
[17] C.J. Morgan, R.R. Vallance, E.R. Marsh, Micro machining glass with polycrystalline diamond tools shaped by micro electro discharge machining, J. Micromech. Microeng. 14 (2004) 1687–1692.
[18] D. Wang, W.S. Zhao, L. Gu, X.M. Kang, A study on micro-hole machining of polycrystalline diamond by micro-electrical discharge machining, J. Mater. Process. Technol. 211 (2011) 3–11.
[19] D.A. Axinte, D.S. Srinivasu, M.C. Kong, P.W. Butler-Smith, Abrasive waterjet cutting of polycrystalline diamond: a preliminary investigation, Int. J. Mach Tools Manu. 49 (2009) 797–803.
[20] S.W. Ding, M. Haas, X. Guo, K. Kuruma, C. Jin, Z. Li, D.D. Awschalom, N. Delegan, F.J. Heremans, A.A. High, M. Loncar, High-Q cavity interface for color centers in thin film diamond, Nat. Commun. 15 (2024) 6358.
[21] A. Toros, M. Kiss, T. Graziosi, H. Sattari, P. Gallo, N. Quack, Precision micro-mechanical components in single crystal diamond by deep reactive ion etching, Microsyst. Nanoeng. 4 (2018) 12.
[22] Z.Z. Li, H. Fan, L. Wang, X. Zhang, X.J. Zhao, Y.H. Yu, Y.S. Xu, Y. Wang, X.J. Wang, S. Juodkazis, Q.D. Chen, H.B. Sun, Super-stealth dicing of transparent solids with nanometric precision, Nat. Photonics 18 (2024) 799–808.
[23] N.C. Golota, D. Preiss, Z.P. Fredin, P. Patil, D.P. Banks, S. Bahri, R.G. Griffin, N. Gershenfeld, High aspect ratio diamond nanosecond laser machining, Appl. Phys. A-Mater. 129 (2023) 490.
[24] Y.L. Liao, F.L. Zhang, P. Wang, X.Z. Xie, Y.M. Zhou, D.L. Xie, Experimental study on fabricating micro-hole arrays on CVD diamond film using a nanosecond pulsed laser, J. Superhard Mater. 43 (2021) 248–260.
[25] A. Savvin, A. Dormidonov, E. Smetanina, V. Mitrokhin, E. Lipatov, D. Genin, S. Potanin, A. Yelisseyev, V. Vins, NV– diamond laser, Nat. Commun. 12 (2021) 7118.
[26] Y. Chen, P.S. Salter, S. Knauer, L. Weng, A.C. Frangeskou, C.J. Stephen, S. N. Ishmael, P.R. Dolan, S. Johnson, B.L. Green, G.W. Morley, M.E. Newton, J. G. Rarity, M.J. Booth, J.M. Smith, Laser writing of coherent colour centres in diamond, Nat. Photonics 11 (2016) 77–80.
[27] M. Fujiwara, S. Inoue, S.-I. Masuno, H. Fu, S. Tokita, M. Hashida, N. Mizuochi, Creation of NV centers over a millimeter-sized region by intense single-shot ultrashort laser irradiation, APL Photonics 8 (2023) 036108.
[28] S.D. Janssens, D. Vázquez-Cortés, B. Sutisna, E. Fried, Direct femtosecond laser writing of nanochannels by carbon allotrope transformation, Carbon 215 (2023) 118455.
[29] H. Hirai, H. Hidai, S. Matsusaka, A. Chiba, Y. Mokuno, M. Yamaguchi, N. Morita, Diamond slicing using ultrashort laser-induced graphitization and additional nanosecond laser illumination, Diamond Relat. Mater. 96 (2019) 126–133.
[30] J.G. Zhao, C. Zhang, F. Liu, G.J. Cheng, Understanding femtosecond laser internal scribing of diamond by atomic simulation: phase transition, structure and property, Carbon 175 (2021) 352–363.

[31] M.N. Qu, T. Jin, G.Z. Xie, R. Cai, Developing a novel binderless diamond grinding wheel with femtosecond laser ablation and evaluating its performance in grinding soft and brittle materials, J. Mater. Process. Technol. 275 (2020) 116359.
[32] C.I.H. Ashby, C.C. Mitchell, J. Han, N.A. Missert, P.P. Provencio, D.M. Follstaedt, G.M. Peake, L. Griego, Low-dislocation-density GaN from a single growth on a textured substrate, Appl. Phys. Lett. 77 (2000) 3233–3235.
[33] B. Ali, I.V. Litvinyuk, M. Rybachuk, Femtosecond laser micromachining of diamond: current research status, applications and challenges, Carbon 179 (2021) 209–226.
[34] M. Girolami, A. Bellucci, M. Mastellone, S. Orlando, V. Valentini, R.M. Montereali, M.A. Vincenti, R. Polini, D.M. Trucchi, Impact of Laser Wavelength on the Optical and Electronic Properties of Black Diamond, Physica Status Solidi (a) 214 (2017).
[35] G.C.B. Lee, S. Su, J. Li, K. Sugden, N. Roohpour, H. Yan, H. Ye, Analysis of femtosecond laser surface patterning on bulk single-crystalline diamond, J. Exp. Nanosci. 7 (2012) 662–672.
[36] M. Shinoda, R.R. Gattass, E. Mazur, Femtosecond laser-induced formation of nanometer-width grooves on synthetic single-crystal diamond surfaces, J. Appl. Phys. 105 (2009) 053102.
[37] P. Calvani, A. Bellucci, M. Girolami, S. Orlando, V. Valentini, A. Lettino, D. M. Trucchi, Optical properties of femtosecond laser-treated diamond, Appl. Phys. A 117 (2014) 25–29.
[38] P. Calvani, A. Bellucci, M. Girolami, S. Orlando, V. Valentini, R. Polini, D. M. Trucchi, Black diamond for solar energy conversion, Carbon 105 (2016) 401–407.
[39] A. Bellucci, P. Calvani, M. Girolami, S. Orlando, R. Polini, D.M. Trucchi, Optimization of black diamond films for solar energy conversion, Appl. Surf. Sci. 380 (2016) 8–11.
[40] M. Mastellone, A. Bellucci, M. Girolami, V. Serpente, R. Polini, S. Orlando, A. Santagata, E. Sani, F. Hitzel, D.M. Trucchi, Deep-subwavelength 2D periodic surface nanostructures on diamond by double-pulse femtosecond laser irradiation, Nano Lett. 21 (2021) 4477–4483.
[41] S. Plimpton, Fast parallel algorithms for short-range molecular-dynamics, J. Comput. Phys. 117 (1995) 1–19.
[42] A. Nakano, Parallel multilevel preconditioned conjugate-gradient approach to variable-charge molecular dynamics, Comput. Phys. Commun. 104 (1997) 59–69.
[43] Q. Spreiter, M. Walter, Classical molecular dynamics simulation with the Velocity Verlet algorithm at strong external magnetic fields, J. Comput. Phys. 152 (1999) 102–119.
[44] J. Tersoff, Empirical interatomic potential for carbon, with applications to amorphous-carbon, Phys. Rev. Lett. 61 (1988) 2879–2882.
[45] J. Feng, J. Wang, H. Liu, Y. Sun, X. Fu, S. Ji, Y. Liao, Y. Tian, A review of an investigation of the ultrafast laser processing of brittle and hard materials, Materials 17 (2024) 3657.
[46] V.P. Krainov, A.S. Roshchupkin, Dynamics of the Coulomb explosion of large hydrogen iodide clusters irradiated by superintense ultrashort laser pulses, Phys. Rev. A 64 (2001) 063204.
[47] R. Stoian, A. Rosenfeld, D. Ashkenasi, I.V. Hertel, N.M. Bulgakova, E.E. B. Campbell, Surface charging and impulsive ion ejection during ultrashort pulsed laser ablation, Phys. Rev. Lett. 88 (2002) 097603.
[48] K.K. Thornber, Applications of scaling to problems in high-field electronic transport, J. Appl. Phys. 52 (1981) 279–290.
[49] Y. Ogawa, M. Ota, K. Nakamoto, T. Fukaya, M. Russell, T.I. Zohdi, K. Yamazaki, H. Aoyama, A study on machining of binder-less polycrystalline diamond by femtosecond pulsed laser for fabrication of micro milling tools, CIRP Ann. 65 (2016) 245–248.
[50] M. Girolami, A. Bellucci, P. Calvani, S. Orlando, V. Valentini, D.M. Trucchi, Raman investigation of femtosecond laser-induced graphitic columns in single-crystal diamond, Appl. Phys. A Mater. Sci. Process. 117 (2014) 143–147.
[51] R. Ramamurti, V. Shanov, R.N. Singh, S. Mamedov, P. Boolchand, Raman spectroscopy study of the influence of processing conditions on the structure of polycrystalline diamond films, J. Vac. Sci. Technol. A 24 (2006) 179–189.
[52] A.C. Ferrari, J. Robertson, Origin of the1150−cm−1Raman mode in nanocrystalline diamond, Phys. Rev. B 63 (2001) 121405.
[53] G. Yan, Y. Wu, D. Cristea, F. Lu, Y. Wang, D. Zhao, M. Tierean, L. Liu, Machining performance of hard-brittle materials by multi-layer micro-nano crystalline diamond coated tools, Results in Physics 13 (2019) 102303.
[54] T. Okada, T. Tomita, T. Ueki, Y. Masai, Y. Bando, Y. Tanaka, Femtosecond-laser-induced modifications on the surface of a single-crystalline diamond, Jpn. J. Appl. Phys. 56 (2017) 112701.